MONTE CARLO MODELLING OF AN X-RAY CHAMBER FOR PROVIDING INACTIVATION EXPOSURES TO VIRUSES

J S Eakins[1,*], B Afrough[2] and R Hewson[2]

[1] *Public Health England (PHE) Centre for Radiation, Chemical and Environmental Hazards (CRCE), Chilton, Didcot, UK*
[2] *Public Health England National Infection Service, Porton Down, Salisbury, Wiltshire, UK*

* jonathan.eakins@phe.gov.uk

ABSTRACT

The Monte Carlo radiation transport code MCNP6 has been used to model dosimetry for biological pathogen samples placed within a MultiRad 225 irradiation chamber, in order to inform virus deactivation protocols. Full characterizations of the photon spectra generated by the chamber's X-ray tube were achieved for both 190 kV and 220 kV potentials, with and without aluminium and copper beam filters of different thicknesses. Dose rate maps to air and water within the chamber were then derived, along with corresponding conversion coefficient data. The maps were determined for samples located both on a shelf and on a dry ice refrigeration chamber, at different distances from the source. The potential depth-dose profiles through samples were also investigated. The optimum choice of filter for use in virus inactivation procedures will rely on a compromise between dose homogeneity and dose rate.

1. INTRODUCTION

Different biological pathogens are naturally associated with different hazards and risks to scientists working with them. In the United States and much of the European Union, laboratories in which work is performed on biological pathogens are categorized into one of four 'biosafety levels'. These levels denote the maximum degree of risk posed by the pathogens permitted within the laboratory, with Level 1 being the lowest risk and Level 4 being the greatest. Accordingly, the higher biosafety levels are associated with enhanced protection features designed to ensure the complete containment of the pathogen and maximize the safety of personnel, such as sophisticated filtration systems and isolation facilities, and the requirement that workers comply with stringent safety procedures and at all times wear sealed body-suits with increased atmospheric pressures (i.e. 'positive pressure'). An alternative but related approach is adopted in the United Kingdom, where pathogens are categorized into hazard groups (1-4) that designate the type of containment required, up to Containment Level 4 (CL4) for HG4 viruses. The UK does not contain workers in suits but instead uses CL3 and CL4 laboratory infrastructure to contain pathogens, with regulations stipulating that such pathogens must be handled within primary containment; consequently, such work is performed in microbiological safety cabinets or cabinet-lines. Nevertheless, in both approaches the much stricter requirements for a higher risk pathogen make routine work with it more challenging than for a lower risk one, and also make the required laboratory infrastructures more expensive to build and maintain. For these reasons, it is advantageous if the biosafety classification or containment level for a given pathogen of interest can be somehow 'downgraded' in a safe and reliable way: this might permit research on it to be conducted using less-restrictive practices and fewer time-consuming control protocols, and in a less expensive environment. Ultimately, this could greatly reduce the cost of research into highly dangerous

pathogens such as Crimean–Congo haemorrhagic fever virus, Lassa fever, viruses from the Ebola family, and many other pathogens that are constantly spilling over into human populations from wildlife reservoirs. It could also drastically advance the rate at which pathogens can be investigated, which would be of clear benefit for new or emerging viruses, with the SARS-CoV-2 pandemic in 2020 being a globally obvious example.

A suggested means of achieving pathogen inactivation is to expose it to a specific dose of ionizing radiation. The optimum dose must be sufficient to render the pathogen biologically non-infectious, but not enough to destroy its structural integrity, such that research on it would still be insightful and accurate. This approach has been attempted previously using radionuclides [Sullivan *et al*, 1971; Elliot *et al*, 1982], but these sources of ionizing radiation are themselves associated with drawbacks, such as security concerns, decay, and waste management; indeed, the UK Government, along with other countries, is currently investigating ways of replacing the radionuclide irradiators used in radiobiology for precisely these reasons [Barnard *et al*, 2020]. Moreover, although filters may potentially be added to change the characteristics of radiation, emission from a radionuclide source is essentially of fixed quality. X-rays, produced using a standard set-up with a vacuum tube that accelerates electrons from a cathode onto a metal anode, do not have the same disadvantages. Furthermore, by varying the X-ray tube potential and beam current, it is possible to fine tune the radiation field so that it better matches the precise dosimetry requirements.

Public Health England (PHE) has recently purchased a standalone X-ray irradiation chamber in order to investigate the viability of its use for pathogen inactivation. Clearly, the success of the approach relies upon the accuracy with which the doses may be delivered and quantified within the chamber, which in turn requires full characterization of the radiation field with respect to various relevant parameters. The current document describes such a characterization, achieved via an extensive programme of Monte Carlo modelling. The key outcomes from the wider study, along with the results of experiments subsequently conducted with the X-ray chamber to inactivate biological pathogens, have been published recently elsewhere [Afrough *et al*, 2020].

2. IRRADIATION CONDITIONS

2.1 Irradiation Chamber

The X-ray irradiation chamber purchased by PHE is a MultiRad 225 unit[1], manufactured and supplied by Precision X-rays®. A technical diagram of the chamber is shown in Figure 1. Schematically, the irradiator incorporates an X-ray tube positioned above a large, lead-shielded, air-filled cavity, from which it is separated by a 0.8 mm thick beryllium window. The X-ray tube is an MXR-225/26 unit manufactured by Comet Group[2] and designed specifically for sterilization applications, and is tuneable by the user, operating with a nominal potential set between 20 and 225 kV and a current between 0.1 and 30 mA. The MXR-225/26 tube incorporates an electron gun directed at 60° towards a tungsten target, with collimation such that a radiation cone with a 37.5° opening-angle passes through the beryllium window. The beryllium effectively removes scattered source electrons whilst leaving the bremsstrahlung photons from the target relatively unperturbed. The beryllium window may optionally be covered by a filter that is fixed directly beneath it; filters supplied by Precision X-rays® are 0.2, 0.5 and 2.0 mm thicknesses of aluminium, and a 0.3 mm thickness of copper. The filter is intended to harden the photon distribution by strongly attenuating the lowest energy components. Samples requiring irradiation may be placed on 4 mm thick aluminium shelves that can be positioned at almost

[1] http://www.faxitron.com/life-sciences-ndt/products/multirad.html
[2] http://www.comet-xray.com/products/x-ray-tubes/tubes/mxr-225-22

any height within the chamber, with the size of the irradiated area then changing geometrically with proximity to the source.

2.2 Exposed samples

During routine use of the irradiator at PHE, each biological sample is contained within ~1 ml of culture medium that is confined within a standard screw-capped polypropylene cryotube vial with 1 mm thick polypropylene walls. Sets of the tubes are double-wrapped in polyethylene bags, each of nominal thickness ~0.114 mm. The exposures are performed in one of two configurations: 1) with the bag placed directly on the shelf; and 2) with the bag placed on top of a dry ice chamber (DIC) located on the shelf. The DIC is used to maintain low temperatures for samples requiring refrigeration during exposure, and comprises a 17.75 cm radius, 9.9 cm high cylinder of aluminium, containing 20 cylindrical cavities, each of 3.15 cm radius and 3.6 cm height, that can be filled with pellets of dry ice.

Target-to-shelf distances of 22.6 cm and 32.5 cm are adopted for the on-shelf exposures and the on-DIC exposures, respectively, resulting in equal target-to-sample distances in the two cases. These distances are considered typical of the likely optimal conditions for the intended exposures, which were chosen as a result of a trade-off between sample size/beam cone geometry and dose rate, and specifically the dose required to enable the best possible recovery over time. On the basis of geometry, the distances are assumed sufficient to expose a circular area of radius ~7-8 cm to the primary photon beam, which is large enough to contain the samples; this assumption is demonstrated explicitly later. For the on-DIC exposures, an additional configuration is also considered with the shelf positioned 22.6 cm from the target: i.e. the same as that used for the on-shelf exposures.

The aluminium bulk of the DIC results in some backscattered radiation that can contribute to the doses to samples placed upon it, in addition to those doses deposited by the primary photon beam incident from above. The circular aluminium shelves are 0.4 cm thick and 20 cm in radius so also cause backscatter, though the magnitude of this component is likely be significantly less than that originating from the DIC, when used. Scatter from the walls, floor and ceiling of the irradiation chamber also perturb the field at a given point-of-test to various extents, all of which are accounted for implicitly by the Monte Carlo modelling.

3. MONTE CARLO MODELLING

The Monte Carlo simulations were performed using the general-purpose radiation transport code MCNP6.1 [Goorley *et al*, 2012]. The aim was to create an accurate model of the irradiation chamber and exposure conditions (Figure 1), using technical data provided by the manufacturers. For reference in the modelling, a Cartesian co-ordinate system was defined with its origin located at the tungsten target, with the *z*-axis vertically above the centre of the shelf, the *x*-axis running from left to right, and the *y*-axis running from front to back from the perspective of an observer looking through the door of the irradiation chamber. These co-ordinate axes and origin will be used for all positions subsequently quoted in this report.

The calculations were run in full coupled electron-photon mode, with detailed physics options selected throughout. However, to maximize simulation efficiency and minimize CPU times, electron transport was 'killed' in all regions outside of the X-ray tube, with absorbed doses then estimated by MCNP '*f6:p*' photon kerma tallies. This use of the kerma approximation in the Monte Carlo modelling was justified on the grounds that secondary electron equilibrium would likely exist at the point-of-test in the real irradiation chamber; the accuracy of this approach is demonstrated later.

For the aluminium and copper filters, densities of 2.71 and 8.94 g/cm^3 respectively were modelled. The X-ray source was modelled as a 2.75 mm radius beam of plane-parallel monoenergetic electrons impinging on an angled target of pure tungsten of density 19.6 g/cm^3. The beam was orientated along the negative *x*-axis, and was hence perpendicular to the vertical (*z*) axis of the irradiation chamber. Production of bremsstrahlung photons in the tungsten was artificially enhanced by setting the '*BNUM*' parameter in MCNP to 10000, with the code then re-weighting the results automatically so that they were not unfairly biased. By default, MCNP normalizes its results to 'per source particle'; in order to usefully relate these data to laboratory dose rates, a realistic beam current of 18.2 mA was supposed for the X-ray tube, which equates to 1.14×10^{17} source electrons per second. This current provides a convenient scaling factor that was adopted for all of the results subsequently presented. However, because of the MCNP normalization, the dose rate results are linearly scalable to any other beam current. Thus, if a dose rate of $\dot{D}$ Gy s^{-1} were to be found at some point-of-test for this 18.2 mA beam current, any alternative current of *J* mA would be expected to yield a dose rate of $[\dot{D} \times (J \div 18.2)]$ Gy s^{-1} at the same location, all other factors being equal.

Of course, results for differing X-ray tube potentials cannot be scaled in the same simple way. Preliminary attention was focussed on an X-ray tube potential of 220 kV, which was assumed equivalent to a monoenergetic incident electron beam of 220 keV in the Monte Carlo modelling. This choice was for operational reasons, having been suggested as preferable for routine use in the laboratory: a potential of 220 kV is close to the upper limit of the MXR-225/26 X-ray tube, and can hence be expected to deliver close to the maximum possible dose rate. This is advantageous for pathogen inactivation, because very high doses of penetrating radiation are typically required to be delivered in a short time interval; for samples requiring exposure on the DIC, it also minimizes the time spent away from more sophisticated refrigeration technology. Higher energy sources can additionally be expected to produce more penetrating photons on average, and hence lead to the most uniform depositions of dose within the sample. Nevertheless, the dosimetric consequences of using a lower tube potential (190 kV) were also later explored in the modelling.

The physical quantity of primary relevance to biological inactivation is assumed to be the absorbed dose to the pathogen. However, determining this at the molecular level is effectively impossible using a macroscopic transport code such as MCNP, which assumes continuum properties for materials rather than fine-grained structures. Moreover, the cultivation media in which samples are contained tend to be highly complex mixtures of organic and inorganic compounds, and may vary from one pathogen to another. In an attempt to mitigate for these limitations, and also to produce a degree of standardization across otherwise differing samples, the 1 ml combination of pathogen + culture medium was represented in the model by water of unit density. This approximation was considered reasonable and scientifically defensible, given the physical and chemical properties typically exhibited by biological samples and the general absence of high atomic number (*Z*) components within them that might impact significantly upon dosimetry. Furthermore, it is not necessarily important that the precise dose to the pathogen might be different from that delivered in water: for the end-purposes of research into inactivation, it is likely sufficient just to benchmark observed biological effects against the corresponding known calibration dose to water provided by the source.

In general, average kerma values across the whole 1 ml sample of water were tallied, and assumed to be relatable to average doses to the pathogen. Again, this was motivated partly by pragmatism, but is taken to be an adequate approach under the reasonable assumptions that doses will likely be deposited fairly uniformly within the samples in the real scenario, and that the pathogen will be evenly mixed and circulating freely within it during exposure: irradiations will be performed at room temperature, so the water will be in a liquid state. The first of these assumptions was subsequently

investigated by splitting the water into ten 0.1 ml (i.e. 1 mm thick) layers and considering the dose to each, as discussed later.

Free-in-air doses at the points of test were also obtained by changing the materials of the sample regions within the model from plastic-covered water to air, and re-running the calculations. These results are of dosimetric interest in themselves, but also because they mimic the quantity measured by ion chambers. It will thus be possible in the future to benchmark the modelled results against physical experiments. These modelled data may also be employed to generate conversion factors that could subsequently be used to relate measured doses in air to the corresponding doses to water (which are in turn assumed proportional to the actual doses to the biological pathogens); an example of their application may be the validation of exposures that have used alternative beam currents.

4. MODELS AND RESULTS

The various simulations that were performed to characterize various aspects of the irradiation chamber are described in turn, along with their results. In general, statistical uncertainties in the output from the Monte Carlo calculations were low (< ~few %); for clarity, these have hence been omitted from many of the subsequent figures. Some exceptions to this were found for the lower dose rate results exhibited at locations around the fringes of the photon beam, but these are less important for the current purposes because biological samples will generally only be exposed within the central regions of the radiation cone.

4.1 Photon energy distributions

The first simulation characterized the energy distributions of the five photon fields that could be supplied: the unfiltered field, and those emerging through the 0.2, 0.5 or 2.0 mm aluminium or 0.3 mm copper filters. This was achieved by defining a 1 cm radius sphere of air positioned a few centimetres beneath the centre of the beryllium window (i.e. at coordinate (0, 0, -12)), and tallying the photon fluence-energy distribution through it using an MCNP '*f4:p*' tally binned into 0.5 keV increments. The results are shown in Figure 2 (*left*).

The unfiltered field demonstrates the expected features from the X-ray source, i.e. a continuum of bremsstrahlung radiation with characteristic peaks at ~10 keV, ~60 keV and ~70 keV originating, respectively, from L, K_α and K_β shell transitions in the tungsten target. These higher-energy peaks are also observed in the filtered fields, but the lower-energy components are increasingly suppressed by additional filtration. Indeed, this suppression is apparent at all energies, albeit to differing extents. Using mass-attenuation data [Hubbell *et al*, 1995] the transmission through the filters may be determined as a function of photon energy, as shown in Figure 2 (*right*) where the rapid decrease at low energies is evident. The copper filter leads to the lowest total fluence overall, being ~42 % that of the unfiltered field, with analogous attenuations to ~87 %, ~80 % and ~65 % caused by the 0.2, 0.5 and 2.0 mm aluminium filters, respectively. These reductions are as expected from the greater attenuating power caused both by increasing mass-thicknesses and the ~2.2× difference in atomic number of copper (Z=29) and aluminium (Z=13). The implication of Figure 2 is therefore an anticipated trade-off: increasing filtration produces a more hardened field, but at the cost of a reduced fluence rate.

Figure 2 indirectly supports the use of the kerma approximation in the modelling. The closest distance between the tungsten target and the shelf is 22.6 cm, which corresponds to the range in air of an electron of energy between 125 and 150 keV [ICRU, 1994]. For the unfiltered 220 kV field, only ~6 %

of the fluence has energy greater than 125 keV and only ~3 % has energy greater than 150 keV, so only a very small fraction of the photons would potentially not be in equilibrium with secondary electrons. Moreover, all other sample positions will be further away than this distance, which will raise the threshold energy below which charged particle equilibrium conditions can be expected; the beryllium window will also contribute to this build-up. Thus, approximate kerma equilibrium can be expected at the sample positions. For the filtered fields, the aluminium or copper will also act as an additional source of build-up, so these conditions can be expected to hold even more completely.

4.2 Dose mapping

The full spatial dose rate map within the irradiation chamber was determined by defining a 20×20 grid of 1×1×1 cm^3 cubes across the shelf or DIC, each filled with water. The entire lattice was then surrounded by a 0.2 cm thickness of polypropylene, itself encased in 0.0228 cm of polyethylene, respectively representing the walls of the cryotubes and polyethylene bags containing the biological samples in the real scenario; these layers of plastic were assumed sufficient to reproduce the correct attenuation of the direct and backscattered components of the field impinging on the samples, with the side-on components assumed dosimetrically negligible. Thus, the modelled configuration was essentially equivalent to exposing 400 samples simultaneously, each of volume 1 ml and each occupying a unique 1 cm^2 grid location within the ranges $-10 \leq x \leq +10$ and $-10 \leq y \leq +10$. The average kerma to each volume was then calculated individually using a set of MCNP *f6:p* tallies: a spatial map of dose deposition to water as a function of (x,y) position was thus obtainable. A corresponding air kerma map was also obtained in a similar way, but with the input file modified such that all relevant volumes were instead filled with air. Dose maps from three different chamber configurations were considered, discussed in turn below.

Results in this section are provided just for the 0.2 mm aluminium-filter configuration. This is because that field was identified as optimum for virus inactivation exposures, as discussed elsewhere [Afrough *et al*, 2020]. However, data analogous to those presented below were also derived for the unfiltered field, and for the 0.5 and 2.0 mm aluminium and 0.3 mm copper filters. These are not shown in this current report for brevity, though may be obtained from the authors on request. Nevertheless, those alternative maps were generally found to exhibit patterns and features similar to those seen in the following figures.

4.2.1 On-shelf dose maps

The 20×20 grid of 1×1×1 cm^3 cubes was positioned on the shelf, which was separated from the source by a distance of 22.6 cm. All five filter configurations were modelled for the 220 kV source of assumed current 18.2 mA.

The resulting dose rates to water for the 0.2 mm aluminium-filtered field at the 400 locations are given in Figure 3a in units of Gy s^{-1}, with the (x,y) co-ordinate label referring to the midpoint of the cube. The corresponding air kerma rates at the same 400 locations are given in Figure 3b. Figure 3c shows the values obtained by dividing the data in Figure 3a by the data in Figure 3b. Figure 3c thus provides 'water dose rate' per 'air kerma rate' conversion coefficients that can be used to convert dose rates obtained by ionization chambers to the corresponding doses to water to which they relate; the coefficients are formally dimensionless, but are given here in units of (Gy s^{-1})/(Gy s^{-1}) as a reminder of the dose quantities. These will be useful in, for example, future benchmarking of the modelled data against measurements, or checking calibrations of the irradiation chamber for alternative beam currents. In general, the statistical uncertainties in the data in the central regions of the dose rate

maps are very small, so have been omitted from Figure 3 for clarity. Around the edges, however, where the dose rates are lower, larger statistical uncertainties are found, albeit still <5 %; the conversion coefficient data at those locations should therefore be treated with slightly more caution, as the uncertainties are compounded.

The results in Figure 3 exhibit a number of trends and features. Firstly, the dose rates generally decrease with distance from the centre of the shelf; this is expected from inverse-square reduction with increased separation from the source, but is also a result of anticipated non-uniformity within the radiation field. However, in the region inside the conical beam of radiation from the source, the dose rates only vary to within a few 10s of percent at most. Secondly, there is a sharp drop in dose rate at distances ~7-8 cm from the centre, which corresponds to the edge of the collimated radiation cone when the shelf is 22.6 cm from the source: $22.6 \times tan(37.5/2) \approx 7.7$ cm. Thus, biological samples placed further than this from the centre of the shelf will receive considerably lower dose rates than samples placed within the cone. Moreover, the dose rates at those locations will result from photons scattered by the shelf, walls, floor and ceiling of the irradiation chamber, the energy distributions of which are not well-characterized and will differ significantly from those shown in Figure 2.

Thirdly, there are also some asymmetries in the dose maps: although the results generally appear invariant under a reflection in the *x*-axis, the same is not true for a reflection in the *y*-axis. That is, for a given distance from the centre of the shelf, it does not matter whether a sample is placed equally towards the back or towards the front of the chamber, but its left-right position will impact the dosimetry, with a sample placed on the right receiving a higher dose rate than its counterpart on the left; preliminary measurements made using ionization chambers confirmed this result. This asymmetry is caused by the asymmetry of the X-ray tube set-up itself: in the adopted coordinate system, the electron beam strikes the tungsten target with velocity vector (-1 0 0), with an angle of 60° also subtended between the face of the target and the positive *x*-axis. If it could be assumed that bremsstrahlung photons were emitted isotropically during interaction events, then due to attenuation within the tungsten the intensity of emergent radiation would be greatest in a direction perpendicular to its surface, i.e. with velocity vector parallel to $(\sqrt{3}/2, 0, -1/2)$, and would fall with increasing angle away from that normal. However, bremsstrahlung emission is actually somewhat anisotropic, with bias towards the forward direction of the electron beam. The true direction of maximum intensity of the emerging photon radiation is therefore the resultant of these two competing factors; in the current circumstance, the photon field is peaked somewhere in the direction of the positive *x*-axis, but no equivalent asymmetry is induced in the +*y* or -*y* directions. Downstream, this leads to proportionally greater dose rates in the right side of the chamber.

The impact of this phenomenon is likely to depend on the choice of filter, affecting the least filtered configurations the most: the filter serves to redistribute and flatten the field to some extent, as well as remove the lowest-energy photon components, which would be most influenced by the tungsten. Although the data are not shown here explicitly, this expectation was confirmed by a comparison of the dose maps for the five configurations. For instance, the dose rate to water at location (6.5, 0.5) was found to be ~34 % higher than that at (-6.5, 0.5) for the unfiltered field, but only ~5 % higher when the 2.0 mm Al filter was included. Inevitably, this lateral asymmetry might impact the choice of filter used in pathogen irradiation studies, with the physical size of the sample dictating the relative importance, or otherwise, of a dose rate gradient across the shelf.

4.2.2 Dry ice chamber dose maps

The 20×20 grid of 1×1×1 cm^3 cubes was positioned on the DIC, the top of which was separated from the source by a distance of 22.6 cm, i.e. the shelf was at z = -32.5 cm for the 9.9 cm high DIC. All five filter configurations were modelled for the 220 kV source of assumed current 18.2 mA.

The resulting dose rates to water at the 400 locations are given in Figure 4a for the 0.2 mm aluminium-filtered field in units of Gy s^{-1}, with the (x,y) co-ordinate label again referring to the midpoint of the cube. The corresponding air kerma rates at the 400 locations are given in Figure 4b. Figure 4c shows the 'water dose rate' per 'air kerma rate' conversion coefficients, in units of (Gy s^{-1})/(Gy s^{-1}), obtained by dividing the data in Figure 4a by the data in Figure 4b. As before, the statistical uncertainties in the data in the central regions of the dose rate maps are small, so have been omitted from the plots for clarity. Also as before, data similar to those presented in Figure 4 were derived for the unfiltered field, and for the 0.5 and 2.0 mm aluminium and 0.3 mm copper filters, but these are not reproduced in this current report for brevity; again, they may be obtained from the authors on request. These alternative maps exhibited patterns similar to those seen in Figure 4.

The results in Figure 4 exhibit trends and features similar to those in Figure 3 for the on-shelf exposures, and are similarly explainable. A comparison between like-for-like dose rate data in Figures 3 and 4 shows that although the on-DIC results are generally higher than the on-shelf results, the differences are typically small. These differences are likely to arise from the increased contribution to dose in the on-DIC case from 'indirect' photons, i.e. those that pass through the sample but are then scattered back into it by the bulk of the aluminium DIC; the 'direct' components of the dose, i.e. that deposited by photons that impinge on the samples from above, are likely to be the same in both cases. However, although both water and air dose rates are seen to be slightly higher for the on-DIC exposures, these systematic increases are nearly cancelled-out when they are divided to generate the conversion coefficients, leading to even smaller differences between the on-shelf and on-DIC values for those latter data.

This observation is important, because the DIC was modelled just as a simple cylinder of aluminium, rather than a complex composite featuring numerous cylindrical wells spatially arranged and inhomogeneously filled by dry ice. Aluminium has a higher Z and density (13 and 2.7 g/cm^3 respectively) than solid carbon dioxide (~7.3 and <2 g/cm^3), so could be expected to backscatter photons more efficiently. But if a solid cylinder of aluminium only leads to small perturbations in the results compared to the on-shelf case, it is reasonable to conclude that a realistic model of the actual DIC would have led to divergences that were even more negligible. The current highly simplified model is thus assumed sufficient to estimate the worst-case dosimetric impact of using the DIC during exposures, with the modelling of more accurate geometries deemed unnecessary. Paraphrasing, although including proper dry ice wells in the DIC model would plausibly lead to some variations from the local dose rates presented in Figure 4, their presence would also be expected to similarly affect samples located across the real DIC. The extents of these variations are likely to be small, however, and may reasonably be ignored; dosimetrically, it is unlikely to matter whether or not a sample is positioned above a dry ice well.

4.2.3 Relocated dry ice chamber dose maps

The shelf was relocated to a distance of z=-22.6 cm from the source, i.e. that used for the on-shelf exposures, and the DIC was positioned upon it with its top then separated from the source by 12.7 cm. The 20×20 grid of 1×1×1 cm^3 cubes was again defined on the DIC, and all five filter configurations were modelled for the 220 kV source of assumed current 18.2 mA.

The resulting dose rates to water at the 400 locations are given in Figure 5a for the 0.2 mm aluminium-filtered field in units of Gy s^{-1}, with the (*x*,*y*) co-ordinate label again referring to the midpoint of the cube. The corresponding air kerma rates at the 400 locations are given in Figure 5b. Figure 5c shows the 'water dose rate' per 'air kerma rate' conversion coefficients obtained by division, in units of (Gy s^{-1})/(Gy s^{-1}). As previously, the statistical uncertainties in the data in the central regions of the dose rate maps are small, so have been omitted from the plots for clarity. Also, as before, analogous data were derived for the unfiltered field, and for the 0.5 and 2.0 mm aluminium and 0.3 mm copper filters; though not shown in this current report, the maps exhibited patterns similar to those seen in Figure 5.

The dose maps in Figure 5 contrast with those in Figure 4 in the expected way, given the differences in geometry between the two cases. Each 1 cm^3 element of the grid in the revised configuration subtends a proportionally larger solid angle at the source than its counterpart in Figure 4, with inverse-square considerations predicting the new dose rate data in the central region to be factors of $(22.6/12.7)^2 \approx 3.2\times$ larger than those for the previous, which is broadly consistent with what is observed. Moreover, there is a much greater variation in dose rates with increasing distance from the centre than before, with the edge of the radiation cone located at $12.7 \times tan(37.5/2) \approx 4.3$ cm from this point. Nevertheless, within this central cone the 'water dose rate' per 'air kerma rate' conversion coefficients are generally commensurate with those calculated previously. Poorer agreement is exhibited beyond this cone, as anticipated from the less well-characterized nature of the scattered radiation field.

The kerma conditions of secondary charged particle equilibrium may not be met as well at this shorter distance from the source as they are for the other configurations, with 12.7 cm corresponding to the range in air of a ~100 keV electron [ICRU, 1994]; approximately 14 % of the fluence of the 0.2 mm aluminium-filtered (Figure 2) has energy greater than this. The worst-case impact of this potential breakdown was tested by re-running the unfiltered calculation with electron transport now allowed everywhere inside the irradiation chamber (specifically: all MCNP electron '*importances*' were put to 1 for all '*cells*', reset from 0 previously), and determining the energy deposited in the air cubes using the more accurate MCNP **f8:p,e* event tally; doses to air are likely to be impacted more than doses to water due to internal build-up in the latter. The resulting dose rates to the four central cells with co-ordinates ($\pm$0.5,$\pm$0.5) were found to agree with those obtained previously (*data not shown*) to within ~$\pm$6 %, which was only just resolvable from the larger statistical uncertainties (~4 %) on these **f8:p,e* data. The conclusion is therefore that the potential failure of secondary charged particle equilibrium for the highest energy components of the field does not impact greatly upon the results. Given that this unfiltered configuration represents a worst-case scenario, with the aluminium or copper filters providing significant additional build-up, the conclusion leads to reasonable confidence in the use of the kerma approximation in the work of this sub-section, and indeed also in all of the other models described in this report.

4.3 Depth-dose profiles

The results given in Figures 3-5 are based upon the average doses to $1\times1\times1$ cm^3 cubes of water or air, with the former supposed relatable to the doses to 1 ml biological samples and the latter to the quantities measured by ionization chambers, assuming kerma equilibria. Whilst a uniform spatial distribution of energy deposition within the air volume might be anticipated because of its low density, the same may not necessarily be true for water: heuristically, what comes out of each air cube is much the same as what goes in, but what comes out of each water cube is different from what goes in. This is especially the case for the doses deposited by the lowest energy components of the photon fields, which might be attenuated strongly by passing through 1 cm of a 1 g cm^{-3} material, such that the field becomes 'hardened' as it transits. Moreover, photoelectric interaction cross-sections, and hence mass

energy-absorption coefficients, generally reduce with increasing energy [Hubbell *et al*, 1995]: higher energy photons therefore generally deposit proportionally less dose per unit distance than lower energy photons. A dose profile might therefore exist within the water as a function of depth, and hence by association may also exist within biological samples.

To investigate this, the $1\times1\times1$ cm^3 cube with midpoint coordinates (x=0.5, y=0.5) was sub-divided into a vertical stack of 10 slices, each of thickness 0.1 cm. The on-shelf calculations (z=-22.6 cm) were then re-run, with the kerma rate to water determined in each slice to estimate the depth-dose rate profile through the volume. All five filter configurations were considered, for the 220 kV source of assumed current 18.2 mA. Results for on-DIC exposures are expected to be similar to those on-shelf, and so have not also been determined explicitly; in principle, backscatter from the DIC would serve to enhance dose homogeneity within the water to some extent, although in practice the magnitude of this improvement would likely be low.

Figure 6 (*left*) shows the absolute dose rates in the 10 slices for the five filter configurations. Figure 6 (*right*) shows the same data but normalized in each case to the respective mean result for the entire 1 cm^3 volume, as derived by averaging each dataset in Figure 6 (*left*); these have values of 0.48, 0.40, 0.35, 0.25 and 0.14 Gy s^{-1}, respectively, for the unfiltered, 0.2 , 0.5 , 2.0 mm aluminium and 0.3 mm copper filtered fields. As can be seen, the doses deposited in the first few millimetres of the water are significantly larger than those deposited at greater depths: for the unfiltered field, for example, the average dose deposited in a given time interval at a depth between 0 and 1 mm is over twice that deposited between 9 and 10 mm, and roughly half of the dose is deposited in the shallowest third of the water. Essentially, the 1 cm thickness of water is filtering out the lowest energy components of the spectra, so dose deposition drops rapidly with distance through the water.

For similar reasons, the gradients of the depth-dose profiles are reduced by increasing filtration of the source, which lessens the disparities of their extrema. For the 0.3 mm copper filter, the doses in the 10th and 1st slice were -7 and +7 %, respectively, of the mean dose to the 1 cm^3 water volume, whilst these ranges were -11 and +11 %, -16 and +18 %, and -21 and +29 % for the 2.0, 0.5 and 0.2 mm aluminium filters, respectively, but -29 and +61 % for the unfiltered configuration. These results are expected, because it is the low energy photons that are least penetrating and hence cause the most variation with depth through the water, and adding filtration hardens the field by attenuating these components more effectively than those of higher energies (Figure 2).

The conclusion, therefore, is that by increasing the filtration, a more uniform deposition of dose is achieved with depth throughout the sample, with the less filtered fields leading to disproportionately higher doses at shallower depths. But, of course, that improved uniformity comes at the cost of a reduced dose rate overall. There is thus an obvious trade-off between dose rates and dose uniformity within the sample, with, at its extremes, the unfiltered field leading to the highest dose rates but the greatest inhomogeneity, and the copper filter leading to the lowest dose rates but the greatest homogeneity.

The decision regarding the ideal choice of filter in this context may hence be somewhat sample-dependent. If it may be assumed that a given biological pathogen circulates freely and efficiently within its 1 ml volume of cultivation medium, such that dose gradients within the sample are effectively unimportant and it is sufficient just to consider average doses, a high dose rate unfiltered exposure may be considered optimal, especially if short exposure times are biologically desirable. But if this assumption cannot be made, or if exposure times are not a factor, it may be advantageous to use a configuration with more filtration, such that the large variations in local dose deposition are minimized. Compounding this decision is the expectation that any cultivation medium with much

higher density or *Z* than water would be likely to exhibit depth-dose profiles that are more inhomogeneous than those presented in Figure 6.

As a final aside, the above results of 0.48, 0.40, 0.35, 0.25 and 0.14 Gy s^{-1} for the average dose rates to water at coordinates (*x*=0.5, *y*=0.5) for the unfiltered, 0.2, 0.5 and 2.0 mm aluminium and 0.3 mm copper filtered fields may be used to scale the data shown in Figures 3-5 to obtain indicative maps for filter configurations other than 0.2 mm aluminium. The ratios of these values for the unfiltered, 0.5 and 2.0 mm aluminium and 0.3 mm copper-filtered fields to the value of 0.40 Gy s^{-1} for the 0.2 mm aluminium-filtered field are 1.2×, 0.88×, 0.63× and 0.35×, respectively, and multiplying the data in Figures 3-5 by these factors provides reasonable estimates of the analogous dose rate maps for those other four filter configurations, valid within the central circular regions. Thus, whilst those alternative dose rate map data have not been reproduced explicitly in this report, the interested reader may gain a good handle on them by following this simple heuristic procedure.

4.4 190 kV tube potential

The 220 kV potential is close to the 225 kV maximum that is deliverable by the MultiRad 225, but the X-ray tube is able to operate at much lower voltages. It is therefore of interest to consider the possible dosimetric impacts of using a lower energy source. To that end, a reduced tube potential of 190 kV was considered as a first example (i.e. ~15 % lower than the previous value), and the simulations described above were repeated. Although somewhat arbitrary, this choice of potential is significantly different from 220 kV, whilst also likely to provide dose rates that are plausible for pathogen exposures: 190 kV is therefore considered an approximate minimum that might conceivably be used in the laboratory for irradiation [Afrough *et al*, 2020]. The resulting fluence-energy distributions from the 190 kV source are shown in Figure 7 for the five filter configurations, along with the dose rate to water map and depth-dose profile resulting from on-shelf exposures at *z* = -22.6 with the 0.2 mm aluminium filter. A beam current of 18.2 mA was again adopted for normalization.

Figure 7 may be compared against the analogous data for the 220 kV source (Figures 2, 3 and 6). The total fluence rates for the 190 kV potential are reduced relative to those for the 220 kV potential, and the distributions are generally lower in energy; for the 190 kV potential the bremsstrahlung continua are also slightly less spread-out in energy, with the 220 kV potential naturally generating some higher energy components. These changes are particularly apparent from the *K*- and *L*-shell transition peaks: although they obviously occur at the same energies in the two cases, for the 190 kV potential the magnitudes of the *K* peaks are suppressed whilst, for the unfiltered field, the magnitude of the *L* peak is increased. The lowest energy components are greatly reduced by the increased attenuation from increased filtration. The mean energies of the fields are compared in Table 1.

At a given location on the mapped grid, reducing the beam potential to 190 kV can reduce the absorbed dose rate to water by a significant margin, i.e. up to a few 10s of percent, relative to the 220 kV case. This fall occurs because the photon distribution from the lower potential source is reduced in both fluence and energy. The depth profile of dose deposition in the water is also more non-uniform for 190 kV than for the higher potential, though only by a fairly small amount: per unit time interval, the doses in the 10^{th} and 1^{st} slice are -22 and +33 %, respectively, of the mean dose to the 1 cm^3 water volume with the 190 kV potential, which compares with the previous values of -21 and +29 % for the 220 kV potential. For the thicker filters the differences resulting from using 190 or 220 kV potentials would likely be less than those exhibited here, though conversely would probably be larger for an unfiltered exposure. Overall, therefore, whilst there are no obvious dosimetry advantages to using a tube potential lower than 220 kV for exposing pathogens, there are clear disadvantages: lower dose rates, the need for longer exposure durations for biological samples, poorer photon penetration, and worsened dose inhomogeneity.

5. SUMMARY AND CONCLUSIONS

The general-purpose Monte Carlo radiation transport code MCNP6 was used to provide dosimetry for biological pathogen samples placed within a MultiRad 225 irradiation chamber (Figure 1). A nominal beam current of 18.2 mA was assumed throughout, but all results are linearly scalable to any other current of practical interest. Characterizations of the photon fluence-energy distributions generated by the X-ray tube were achieved for 220 kV and 190 kV beam potentials, for unfiltered and 0.2, 0.5 and 2.0 mm aluminium and 0.3 mm copper filtered configurations (Figures 2 and 7, Table 1). Dose rate maps to 20×20 grids of 1×1×1 cm^3 cubes of water or air were also derived as a function of left-right and front-back position within the chamber, along with corresponding conversion coefficients between the two datasets, for samples located either on-shelf or on-DIC (Figures 3-5). The depth-dose profiles through water were also investigated (Figure 6). Only dose rate maps for the 0.2 mm aluminium filtered field are shown explicitly in this report; analogous maps for the unfiltered, 0.5 and 2.0 mm aluminium and 0.3 mm copper filtered configurations can be obtained from the authors, but reasonable approximations to them may also readily be derived simply by scaling the data within the central regions of Figures 3-5 by factors of 1.2×, 0.88×, 0.63× and 0.35×, respectively. The subsequent measurements using the sample irradiation system, exposures of biological pathogens, and the efficacy of the irradiation techniques for virus inactivation, are described and discussed elsewhere [Afrough *et al*, 2020].

A few general comments and observations may be summarized from the results:

- Increasing the filtration hardens the fluence-energy distribution of the photon field, raising its mean energy whilst decreasing the overall fluence and hence dose rate.

- The dose rate maps from the sources are characterized by a relatively high dose rate region within the 37.5° cone subtended by the collimated source, and a comparatively low dose rate region outside of this that is deposited only by scattered radiation.

- Within the cones a significant left-right asymmetry exists in the dose rates, but no analogous front-back asymmetry. The asymmetry can be shown to reduce with increasing source filtration.

- All other factors being equal, changing the shelf height causes the dose rate at a given location within the central region to vary according to the inverse-square distance between the sample and the source.

- For exposures performed on the aluminium DIC, backscatter does not cause a large perturbation of the doses received.

- Significant gradients occur in the depth-dose profiles through the water, especially for the least filtered fields. This problem is exacerbated for lower tube potentials, which are also associated with lower dose rates in general.

The outcome of these last observations is that the precise dose to water, or indeed the dose to the growing medium and pathogen in the 'real' case, may depend somewhat on the quantity of material inside the cryotube. This might suggest that, for the most accurate dosimetry, a high tube potential in combination with the strongest filtration is preferable, although the latter comes with the heavy penalty of lowering the dose rate. Thicker filters also lead to a more uniform dose map, with a reduced

left-right asymmetry within the radiation cone. However, the presumed distribution and circulation of the pathogen within the medium may mitigate the effects of this to some extent, so will be important factors to consider when choosing the filter, along with any biological constraints on the duration of exposure. In reality, a compromise would therefore be required that balances the perceived benefits of improved dose homogeneity against the drawback of reduced dose rates.

The current work has assumed that the dose rate to water is directly relatable to the dose rate to the pathogen. This assumption was motivated primarily by pragmatism, but is expected to be a scientifically sound notion in general. Moreover, there is scope within the approach for the exact relationship between water and pathogen doses to be relatively loose, with a strict 1:1 proportionality not necessarily required. This is because for the end-purposes of research into virus inactivation it may be acceptable just to calibrate observed biological effects against the equivalent benchmarked doses to water.

Although dose rate maps for all five filter configurations were generated during the modelling campaign, only results for the 0.2 mm aluminium filter have been included explicitly in this report. This focus is because that filter was concluded to be the best option for pathogen exposures overall [Afrough *et al*, 2020]: it provides the highest dose rates apart from those from the unfiltered field, but does not contain as many low-energy photon components as that alternative, and so does not suffer the same effects of field degradation through the sample that lead to large dose gradients. This paper considered a shelf height that was set such that the source-to-sample distance was ~22 cm. Given the 37.5° beam collimation, this provided an approximately 7 cm radius circular region within which the dose rate was relatively high, stable and directed; outside of that central region, the dose was only deposited by scattered radiation. This resultant cone size is roughly optimal for the biological exposures of interest: it is sufficiently large to cover the sets of cryotubes routinely used during pathogen inactivation [Afrough *et al*, 2020], but small enough to minimize inverse-square diminishment of the dose rate and maximize the ratio between the primary and scattered radiation dose components. However, the Monte Carlo modelling methods employed here are readily applicable to other shelving configurations and heights, other tube potentials and filters, and even other types of irradiator from different manufacturers. The present work may thus be viewed as a proof-of-concept that is naturally extendible to meet the emerging needs of future research into pathogen inactivation.

ACKNOWLEDGEMENTS

The authors acknowledge and are grateful to Sarah Durley-White of the Defence Science and Technology Laboratory (Dstl), Porton Down, UK, for her input and collaboration with this project into inactivation of biological pathogens.

REFERENCES

Afrough B, Eakins J, Durley-White S, Dowall S, Findlay-Wilson S, Graham V, Lewandowski K, Carter D, and Hewson R (2020). X-ray inactivation of RNA viruses without loss of biological characteristics. Nature Scientific Reports, 10:21431.

Barnard S, Ainsbury L, Daniels T, Eakins J, Tanner R and Bouffler S (2020). Alternatives to caesium irradiators for biological sciences and blood transfusion services. Public Health England report, CRCE-RED-001-2020.

Elliott, L. H., McCormick, J. B. and Johnson, K. M (1982). Inactivation of Lassa, Marburg, and Ebola viruses by gamma irradiation. J Clin Microbiol 16, 704-708.

Goorley, T. et al (2012). Initial MCNP6 release overview. Nucl. Technol. 180, 298–315. https://doi.org/10.13182 /NT11-135

Health and Safety Executive (HSE) (2013). The Approved List of biological agents. HSE Report MISC208 (rev3).

Hubbell, J. H. and Seltzer, S. M (1995). Tables of X-ray Mass Attenuation Coefficients and Mass Energy-Absorption Coefficients 1 keV to 20 MeV for Elements Z = 1 to 92 and 48 Additional Substances of Dosimetric Interest. NISTIR 5632 (Gaithersburg: NIST, U.S. Dept. of Commerce).

International Commission on Radiation Units and Measurements (ICRU) (1994). Stopping Powers for Electrons and Positions. ICRU Report 37.

Sullivan, R., Fassolitis, A. C., Larkin, E. P., Read, R. B., Jr. and Peeler, J. T (1971). Inactivation of thirty viruses by gamma radiation. Appl Microbiol 22, 61-65.

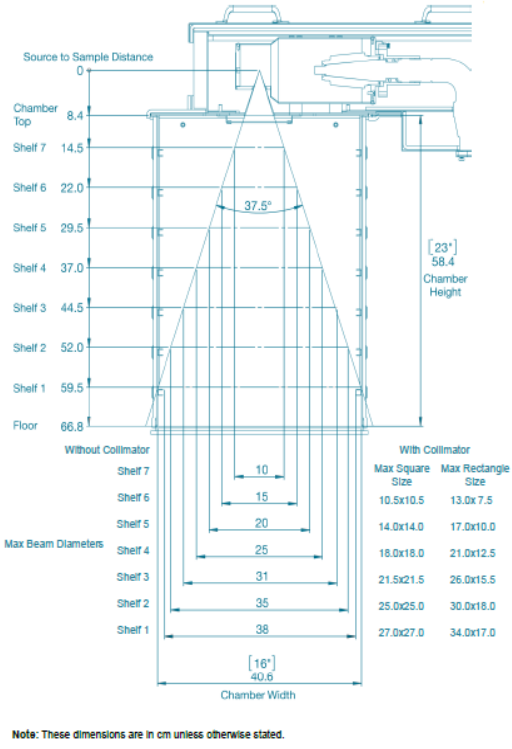

Figure 1: MultiRad 225 irradiation chamber *(*Cross-sectional s*chematic reprinted from the Advanced Users' Manual for the Faxitron MultiRad*, http://www.faxitron.com/life-sciences-ndt/products/multirad.html).

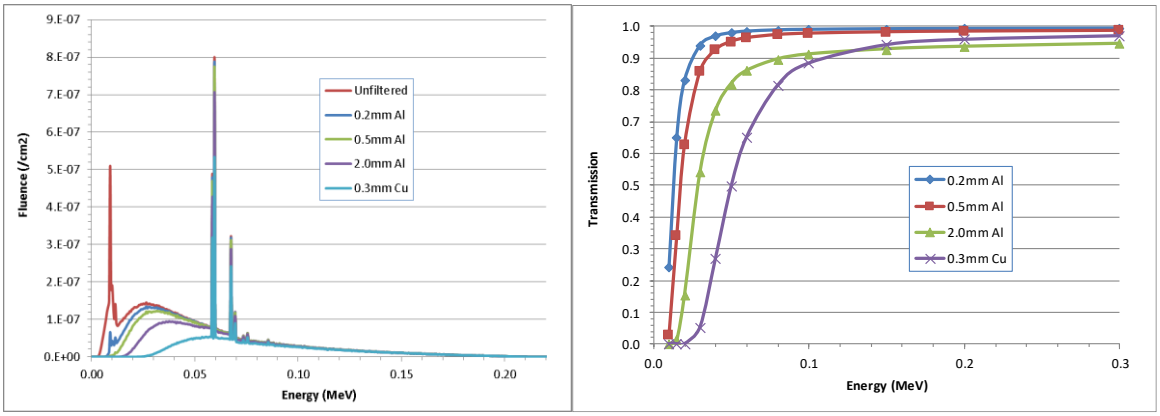

Figure 2: (*Left*) Filtered and unfiltered photon fields for a 220 kV tube potential operating at 18.2 mA; (*Right*) energy-dependent transmission through those filters.

(X,Y)	-9.5	-8.5	-7.5	-6.5	-5.5	-4.5	-3.5	-2.5	-1.5	-0.5	0.5	1.5	2.5	3.5	4.5	5.5	6.5	7.5	8.5
9.5	0.01	0.01	0.01	0.01	0.01	0.01	0.01	0.01	0.01	0.01	0.01	0.01	0.01	0.01	0.01	0.01	0.01	0.00	0.00
8.5	0.01	0.01	0.01	0.01	0.01	0.02	0.02	0.02	0.02	0.03	0.03	0.02	0.02	0.02	0.01	0.01	0.01	0.01	0.00
7.5	0.01	0.01	0.01	0.02	0.02	0.02	0.03	0.07	0.11	0.14	0.15	0.12	0.08	0.04	0.02	0.02	0.01	0.01	0.01
6.5	0.01	0.02	0.02	0.02	0.03	0.06	0.16	0.25	0.29	0.30	0.31	0.30	0.27	0.18	0.08	0.03	0.02	0.01	0.01
5.5	0.02	0.02	0.02	0.03	0.08	0.22	0.29	0.32	0.34	0.35	0.35	0.36	0.35	0.33	0.25	0.10	0.03	0.02	0.01
4.5	0.02	0.02	0.03	0.06	0.22	0.30	0.33	0.34	0.35	0.36	0.37	0.37	0.37	0.37	0.34	0.25	0.08	0.02	0.01
3.5	0.02	0.03	0.04	0.15	0.29	0.32	0.34	0.36	0.37	0.38	0.38	0.39	0.39	0.38	0.37	0.34	0.19	0.04	0.02
2.5	0.03	0.03	0.05	0.24	0.30	0.33	0.35	0.36	0.38	0.39	0.39	0.40	0.40	0.39	0.38	0.37	0.29	0.08	0.02
1.5	0.03	0.03	0.09	0.28	0.31	0.33	0.35	0.37	0.38	0.39	0.40	0.40	0.40	0.40	0.39	0.38	0.34	0.12	0.02
0.5	0.03	0.04	0.12	0.28	0.31	0.34	0.36	0.37	0.38	0.39	0.40	0.41	0.40	0.41	0.39	0.38	0.35	0.15	0.03
-0.5	0.03	0.04	0.12	0.28	0.31	0.33	0.35	0.37	0.39	0.39	0.40	0.40	0.40	0.40	0.39	0.38	0.35	0.15	0.03
-1.5	0.03	0.03	0.09	0.27	0.31	0.34	0.35	0.37	0.38	0.39	0.40	0.40	0.40	0.40	0.40	0.37	0.33	0.12	0.02
-2.5	0.03	0.03	0.06	0.24	0.30	0.33	0.35	0.36	0.38	0.39	0.39	0.40	0.40	0.39	0.39	0.37	0.29	0.08	0.02
-3.5	0.02	0.03	0.04	0.15	0.28	0.32	0.34	0.35	0.37	0.38	0.38	0.39	0.39	0.38	0.37	0.34	0.19	0.04	0.02
-4.5	0.02	0.02	0.03	0.06	0.22	0.30	0.32	0.34	0.35	0.36	0.37	0.37	0.37	0.36	0.35	0.25	0.08	0.02	0.01
-5.5	0.02	0.02	0.02	0.03	0.08	0.22	0.29	0.32	0.34	0.35	0.35	0.35	0.35	0.33	0.25	0.10	0.03	0.02	0.01
-6.5	0.01	0.02	0.02	0.02	0.03	0.06	0.16	0.25	0.29	0.31	0.31	0.30	0.26	0.18	0.08	0.03	0.02	0.01	0.01
-7.5	0.01	0.01	0.01	0.02	0.02	0.02	0.03	0.07	0.11	0.14	0.14	0.12	0.08	0.04	0.02	0.02	0.01	0.01	0.01
-8.5	0.01	0.01	0.01	0.01	0.01	0.02	0.02	0.02	0.02	0.03	0.03	0.03	0.02	0.02	0.01	0.01	0.01	0.01	0.00
-9.5	0.01	0.01	0.01	0.01	0.01	0.01	0.01	0.01	0.01	0.01	0.01	0.01	0.01	0.01	0.01	0.01	0.01	0.00	0.00

Figure 3a: On-shelf dose rates to water (Gy s^{-1}) for the 0.2 mm Al filtered field at position (*x*,*y*) for shelf at *z*=-22.6 cm, 220 kV tube potential and 18.2 mA current.

(X,Y)	-9.5	-8.5	-7.5	-6.5	-5.5	-4.5	-3.5	-2.5	-1.5	-0.5	0.5	1.5	2.5	3.5	4.5	5.5	6.5	7.5	8.5
9.5	0.01	0.01	0.01	0.01	0.01	0.01	0.01	0.02	0.02	0.02	0.02	0.02	0.01	0.01	0.01	0.01	0.01	0.01	0.01
8.5	0.01	0.01	0.01	0.02	0.02	0.02	0.02	0.02	0.02	0.03	0.03	0.02	0.02	0.02	0.01	0.01	0.01	0.01	0.01
7.5	0.01	0.02	0.02	0.02	0.02	0.02	0.03	0.08	0.13	0.17	0.18	0.14	0.09	0.04	0.02	0.02	0.01	0.01	0.01
6.5	0.02	0.02	0.02	0.03	0.03	0.07	0.19	0.30	0.35	0.37	0.38	0.38	0.33	0.23	0.09	0.03	0.02	0.01	0.01
5.5	0.02	0.03	0.03	0.03	0.08	0.26	0.34	0.37	0.40	0.42	0.42	0.43	0.43	0.41	0.31	0.12	0.03	0.02	0.01
4.5	0.03	0.03	0.03	0.06	0.25	0.34	0.37	0.40	0.42	0.43	0.45	0.45	0.45	0.45	0.43	0.32	0.09	0.02	0.01
3.5	0.03	0.03	0.04	0.17	0.33	0.36	0.38	0.41	0.43	0.45	0.46	0.47	0.47	0.47	0.46	0.43	0.24	0.04	0.02
2.5	0.03	0.04	0.06	0.28	0.34	0.37	0.40	0.42	0.44	0.45	0.47	0.48	0.48	0.47	0.47	0.46	0.37	0.09	0.02
1.5	0.04	0.04	0.10	0.31	0.35	0.37	0.40	0.43	0.45	0.46	0.48	0.48	0.49	0.49	0.49	0.48	0.43	0.15	0.02
0.5	0.04	0.04	0.14	0.32	0.35	0.38	0.40	0.43	0.45	0.46	0.48	0.49	0.50	0.49	0.49	0.48	0.45	0.20	0.03
-0.5	0.04	0.04	0.14	0.32	0.35	0.38	0.41	0.43	0.45	0.46	0.48	0.48	0.49	0.49	0.49	0.48	0.45	0.20	0.03
-1.5	0.04	0.04	0.10	0.31	0.35	0.37	0.40	0.43	0.45	0.46	0.47	0.48	0.49	0.49	0.48	0.48	0.43	0.15	0.02
-2.5	0.03	0.04	0.06	0.28	0.34	0.37	0.39	0.42	0.44	0.45	0.47	0.48	0.48	0.48	0.48	0.46	0.37	0.09	0.02
-3.5	0.03	0.04	0.04	0.17	0.33	0.36	0.39	0.41	0.42	0.45	0.46	0.47	0.47	0.47	0.46	0.43	0.24	0.04	0.02
-4.5	0.03	0.03	0.03	0.06	0.25	0.34	0.37	0.39	0.41	0.43	0.44	0.45	0.45	0.45	0.43	0.32	0.09	0.02	0.01
-5.5	0.02	0.03	0.03	0.03	0.09	0.25	0.34	0.37	0.40	0.41	0.42	0.43	0.43	0.41	0.32	0.12	0.03	0.01	0.01
-6.5	0.02	0.02	0.02	0.03	0.03	0.07	0.19	0.29	0.35	0.37	0.38	0.37	0.33	0.23	0.09	0.03	0.02	0.01	0.01
-7.5	0.02	0.02	0.02	0.02	0.02	0.02	0.03	0.07	0.13	0.17	0.17	0.14	0.09	0.04	0.02	0.02	0.01	0.01	0.01
-8.5	0.01	0.01	0.01	0.01	0.02	0.02	0.02	0.02	0.02	0.03	0.03	0.02	0.02	0.02	0.01	0.01	0.01	0.01	0.01
-9.5	0.01	0.01	0.01	0.01	0.01	0.01	0.01	0.02	0.02	0.02	0.02	0.02	0.01	0.01	0.01	0.01	0.01	0.01	0.01

Figure 3b: On-shelf air kerma rates (Gy s^{-1}) for the 0.2 mm Al filtered field at position (*x*,*y*) for shelf at *z*=-22.6 cm, 220 kV tube potential and 18.2 mA current.

(X,Y)	-9.5	-8.5	-7.5	-6.5	-5.5	-4.5	-3.5	-2.5	-1.5	-0.5	0.5	1.5	2.5	3.5	4.5	5.5	6.5	7.5	8.5
9.5	0.64	0.69	0.71	0.71	0.76	0.77	0.80	0.86	0.85	0.91	0.92	0.87	0.92	0.83	0.86	0.86	0.86	0.83	0.71
8.5	0.70	0.70	0.77	0.78	0.80	0.86	0.93	0.93	1.02	0.99	1.01	1.04	1.00	0.99	0.91	0.95	0.88	0.91	0.81
7.5	0.72	0.72	0.73	0.85	0.87	0.98	0.99	0.91	0.86	0.83	0.83	0.82	0.86	0.95	1.04	1.03	0.93	0.86	0.76
6.5	0.70	0.74	0.77	0.84	0.97	0.93	0.85	0.84	0.83	0.82	0.82	0.80	0.80	0.80	0.87	1.06	1.05	0.90	0.88
5.5	0.73	0.76	0.81	0.91	0.92	0.86	0.86	0.86	0.84	0.83	0.84	0.82	0.81	0.80	0.78	0.83	1.07	0.99	0.84
4.5	0.75	0.76	0.87	0.92	0.87	0.87	0.87	0.86	0.85	0.85	0.84	0.82	0.82	0.81	0.80	0.77	0.85	1.07	0.96
3.5	0.75	0.82	0.96	0.88	0.87	0.88	0.88	0.87	0.85	0.85	0.83	0.83	0.82	0.81	0.80	0.79	0.79	1.00	1.06
2.5	0.73	0.81	0.92	0.88	0.89	0.89	0.88	0.86	0.85	0.85	0.83	0.83	0.83	0.82	0.81	0.79	0.77	0.85	1.07
1.5	0.70	0.84	0.90	0.88	0.89	0.89	0.88	0.86	0.85	0.85	0.83	0.83	0.82	0.82	0.80	0.80	0.78	0.80	1.07
0.5	0.72	0.83	0.89	0.89	0.89	0.89	0.88	0.86	0.85	0.85	0.84	0.83	0.81	0.82	0.80	0.79	0.78	0.78	1.04
-0.5	0.75	0.86	0.90	0.89	0.90	0.89	0.87	0.87	0.86	0.85	0.84	0.83	0.82	0.81	0.80	0.79	0.78	0.78	1.02
-1.5	0.74	0.82	0.90	0.89	0.89	0.89	0.88	0.87	0.85	0.85	0.84	0.84	0.82	0.81	0.83	0.79	0.77	0.81	1.00
-2.5	0.74	0.80	0.92	0.87	0.89	0.88	0.88	0.87	0.86	0.85	0.84	0.83	0.82	0.81	0.81	0.79	0.78	0.87	1.08
-3.5	0.72	0.76	0.90	0.88	0.87	0.87	0.87	0.87	0.86	0.85	0.84	0.83	0.82	0.81	0.81	0.79	0.77	1.02	0.98
-4.5	0.70	0.76	0.86	0.95	0.87	0.87	0.87	0.87	0.86	0.85	0.84	0.83	0.82	0.81	0.80	0.77	0.84	1.04	1.01
-5.5	0.72	0.74	0.82	0.93	0.91	0.86	0.86	0.87	0.85	0.84	0.83	0.82	0.82	0.80	0.78	0.84	1.01	1.04	0.94
-6.5	0.71	0.73	0.78	0.84	0.96	0.92	0.85	0.86	0.83	0.83	0.83	0.81	0.80	0.80	0.85	1.02	0.97	0.91	0.82
-7.5	0.70	0.72	0.72	0.80	0.88	0.96	1.02	0.91	0.86	0.85	0.83	0.84	0.87	0.92	1.02	1.00	0.92	0.87	0.81
-8.5	0.69	0.73	0.76	0.79	0.85	0.88	0.95	1.02	1.02	1.01	1.02	1.06	0.98	0.97	0.93	0.89	0.83	0.79	0.71
-9.5	0.68	0.69	0.75	0.77	0.72	0.82	0.81	0.83	0.89	0.95	0.89	0.91	0.94	0.92	0.86	0.81	0.78	0.74	0.74

Figure 3c: On-shelf air kerma to water dose ((Gy s^{-1})/(Gy s^{-1})) conversion coefficients for the 0.2 mm Al filtered field at position (*x*,*y*) for shelf at *z*=-22.6 cm, 220 kV tube potential and 18.2 mA current.

(X,Y)	-9.5	-8.5	-7.5	-6.5	-5.5	-4.5	-3.5	-2.5	-1.5	-0.5	0.5	1.5	2.5	3.5	4.5	5.5	6.5	7.5	8.5
9.5	0.01	0.01	0.01	0.01	0.01	0.01	0.01	0.02	0.02	0.02	0.02	0.02	0.02	0.01	0.01	0.01	0.01	0.01	0.00
8.5	0.01	0.01	0.01	0.01	0.02	0.02	0.02	0.03	0.03	0.03	0.03	0.03	0.03	0.02	0.02	0.01	0.01	0.01	0.01
7.5	0.01	0.01	0.02	0.02	0.02	0.03	0.04	0.08	0.12	0.15	0.15	0.13	0.08	0.05	0.03	0.02	0.01	0.01	0.01
6.5	0.01	0.02	0.02	0.03	0.03	0.07	0.17	0.26	0.30	0.32	0.32	0.31	0.28	0.19	0.08	0.03	0.02	0.01	0.01
5.5	0.02	0.02	0.03	0.04	0.08	0.23	0.30	0.34	0.35	0.36	0.37	0.37	0.36	0.34	0.26	0.10	0.03	0.02	0.01
4.5	0.02	0.03	0.03	0.07	0.23	0.31	0.34	0.35	0.37	0.38	0.39	0.39	0.39	0.38	0.35	0.26	0.08	0.03	0.02
3.5	0.03	0.03	0.04	0.16	0.30	0.33	0.35	0.37	0.38	0.39	0.40	0.40	0.40	0.40	0.38	0.35	0.20	0.04	0.02
2.5	0.03	0.04	0.06	0.25	0.31	0.34	0.36	0.38	0.39	0.40	0.41	0.41	0.41	0.40	0.40	0.38	0.30	0.08	0.02
1.5	0.03	0.04	0.10	0.29	0.32	0.35	0.37	0.39	0.40	0.41	0.41	0.42	0.42	0.41	0.41	0.39	0.35	0.13	0.03
0.5	0.03	0.04	0.13	0.29	0.33	0.35	0.37	0.39	0.40	0.41	0.42	0.42	0.42	0.42	0.41	0.39	0.36	0.16	0.03
-0.5	0.03	0.04	0.13	0.29	0.33	0.35	0.37	0.39	0.40	0.41	0.42	0.42	0.42	0.41	0.41	0.39	0.36	0.16	0.03
-1.5	0.03	0.04	0.10	0.28	0.32	0.35	0.37	0.38	0.40	0.41	0.41	0.42	0.42	0.41	0.40	0.39	0.34	0.13	0.03
-2.5	0.03	0.04	0.06	0.25	0.31	0.34	0.36	0.38	0.39	0.40	0.41	0.41	0.41	0.40	0.40	0.38	0.30	0.08	0.02
-3.5	0.03	0.03	0.04	0.16	0.30	0.33	0.35	0.37	0.38	0.39	0.40	0.40	0.40	0.40	0.39	0.35	0.19	0.04	0.02
-4.5	0.02	0.03	0.03	0.06	0.23	0.31	0.34	0.36	0.37	0.38	0.39	0.39	0.39	0.38	0.36	0.26	0.08	0.03	0.02
-5.5	0.02	0.02	0.03	0.04	0.08	0.23	0.31	0.33	0.35	0.36	0.37	0.37	0.36	0.34	0.26	0.10	0.03	0.02	0.01
-6.5	0.02	0.02	0.02	0.03	0.03	0.07	0.17	0.26	0.30	0.32	0.32	0.31	0.27	0.19	0.08	0.03	0.02	0.01	0.01
-7.5	0.01	0.01	0.02	0.02	0.02	0.03	0.04	0.08	0.12	0.15	0.15	0.13	0.08	0.05	0.03	0.02	0.01	0.01	0.01
-8.5	0.01	0.01	0.01	0.01	0.02	0.02	0.02	0.03	0.03	0.03	0.03	0.03	0.02	0.02	0.02	0.01	0.01	0.01	0.01
-9.5	0.01	0.01	0.01	0.01	0.01	0.01	0.01	0.02	0.02	0.02	0.02	0.02	0.01	0.01	0.01	0.01	0.01	0.01	0.00

Figure 4a: On-DIC dose rates to water (Gy s^{-1}) for the 0.2 mm Al filtered field at position (*x*,*y*) for shelf at *z*=-32.5 cm, 220 kV tube potential and 18.2 mA current.

(X,Y)	-9.5	-8.5	-7.5	-6.5	-5.5	-4.5	-3.5	-2.5	-1.5	-0.5	0.5	1.5	2.5	3.5	4.5	5.5	6.5	7.5	8.5
9.5	0.01	0.01	0.01	0.01	0.01	0.02	0.02	0.02	0.02	0.02	0.02	0.02	0.02	0.01	0.01	0.01	0.01	0.01	0.01
8.5	0.01	0.02	0.02	0.02	0.02	0.02	0.02	0.03	0.03	0.03	0.03	0.03	0.02	0.02	0.02	0.01	0.01	0.01	0.01
7.5	0.02	0.02	0.02	0.02	0.02	0.03	0.04	0.08	0.14	0.18	0.18	0.15	0.09	0.05	0.03	0.02	0.01	0.01	0.01
6.5	0.02	0.02	0.03	0.03	0.03	0.07	0.20	0.31	0.36	0.38	0.39	0.38	0.34	0.23	0.10	0.03	0.02	0.01	0.01
5.5	0.02	0.03	0.03	0.04	0.09	0.26	0.35	0.39	0.41	0.43	0.43	0.44	0.44	0.42	0.33	0.13	0.03	0.02	0.01
4.5	0.03	0.03	0.04	0.07	0.26	0.35	0.38	0.41	0.43	0.44	0.46	0.46	0.47	0.46	0.44	0.33	0.09	0.03	0.02
3.5	0.03	0.04	0.05	0.18	0.34	0.37	0.40	0.42	0.45	0.46	0.47	0.48	0.49	0.48	0.47	0.45	0.25	0.04	0.02
2.5	0.04	0.04	0.07	0.28	0.35	0.38	0.41	0.44	0.46	0.47	0.48	0.49	0.50	0.49	0.49	0.48	0.38	0.10	0.02
1.5	0.04	0.05	0.11	0.32	0.36	0.39	0.42	0.44	0.46	0.48	0.49	0.50	0.50	0.50	0.50	0.49	0.44	0.16	0.03
0.5	0.04	0.05	0.14	0.33	0.36	0.39	0.42	0.45	0.47	0.48	0.50	0.50	0.51	0.51	0.50	0.49	0.46	0.20	0.03
-0.5	0.04	0.05	0.15	0.33	0.36	0.39	0.42	0.44	0.47	0.48	0.50	0.50	0.51	0.50	0.50	0.49	0.46	0.20	0.03
-1.5	0.04	0.05	0.11	0.32	0.36	0.39	0.42	0.44	0.46	0.48	0.49	0.50	0.50	0.51	0.49	0.49	0.44	0.16	0.03
-2.5	0.04	0.04	0.07	0.29	0.35	0.38	0.41	0.43	0.46	0.47	0.48	0.49	0.50	0.49	0.49	0.48	0.38	0.09	0.02
-3.5	0.03	0.04	0.05	0.18	0.34	0.37	0.40	0.42	0.44	0.46	0.47	0.48	0.49	0.48	0.48	0.44	0.25	0.04	0.02
-4.5	0.03	0.03	0.04	0.07	0.26	0.35	0.39	0.41	0.43	0.45	0.46	0.47	0.47	0.46	0.45	0.33	0.09	0.03	0.02
-5.5	0.03	0.03	0.03	0.04	0.09	0.27	0.36	0.39	0.41	0.42	0.44	0.44	0.44	0.42	0.32	0.12	0.03	0.02	0.01
-6.5	0.02	0.02	0.03	0.03	0.03	0.08	0.20	0.31	0.36	0.38	0.39	0.38	0.34	0.23	0.10	0.03	0.02	0.01	0.01
-7.5	0.02	0.02	0.02	0.02	0.02	0.03	0.04	0.08	0.14	0.18	0.18	0.15	0.09	0.05	0.03	0.02	0.02	0.01	0.01
-8.5	0.01	0.01	0.02	0.02	0.02	0.02	0.02	0.03	0.03	0.03	0.03	0.03	0.03	0.02	0.02	0.02	0.01	0.01	0.01
-9.5	0.01	0.01	0.01	0.01	0.01	0.02	0.02	0.02	0.02	0.02	0.02	0.02	0.02	0.01	0.01	0.01	0.01	0.01	0.01

Figure 4b: On-DIC air kerma rates (Gy s^{-1}) for the 0.2 mm Al filtered field at position (*x*,*y*) for shelf at *z*=-32.5 cm, 220 kV tube potential and 18.2 mA current.

(X,Y)	-9.5	-8.5	-7.5	-6.5	-5.5	-4.5	-3.5	-2.5	-1.5	-0.5	0.5	1.5	2.5	3.5	4.5	5.5	6.5	7.5	8.5
9.5	0.70	0.69	0.71	0.72	0.81	0.79	0.84	0.86	0.94	0.91	0.95	0.92	0.94	0.91	0.89	0.86	0.85	0.81	0.74
8.5	0.73	0.71	0.76	0.79	0.88	0.88	0.93	0.95	1.01	1.00	1.02	1.00	1.04	0.97	0.95	0.90	0.86	0.90	0.84
7.5	0.72	0.77	0.79	0.85	0.93	1.00	1.00	0.93	0.87	0.85	0.84	0.84	0.89	0.99	1.06	1.02	0.95	0.87	0.83
6.5	0.72	0.78	0.83	0.87	0.97	0.95	0.87	0.84	0.84	0.83	0.83	0.82	0.81	0.81	0.88	1.03	1.02	0.96	0.85
5.5	0.74	0.77	0.83	0.95	0.91	0.86	0.87	0.86	0.86	0.85	0.85	0.83	0.82	0.80	0.79	0.84	1.03	0.99	0.92
4.5	0.75	0.80	0.89	0.94	0.87	0.88	0.88	0.87	0.86	0.85	0.83	0.83	0.83	0.81	0.80	0.78	0.88	1.04	0.95
3.5	0.76	0.82	0.94	0.88	0.89	0.88	0.88	0.87	0.86	0.86	0.84	0.84	0.83	0.82	0.81	0.79	0.79	0.99	0.99
2.5	0.75	0.83	0.95	0.89	0.89	0.89	0.88	0.87	0.86	0.85	0.84	0.84	0.83	0.82	0.81	0.79	0.78	0.86	1.05
1.5	0.77	0.86	0.91	0.89	0.89	0.89	0.88	0.87	0.87	0.86	0.85	0.84	0.83	0.82	0.81	0.80	0.78	0.81	1.04
0.5	0.76	0.88	0.90	0.90	0.91	0.90	0.88	0.87	0.86	0.85	0.84	0.84	0.83	0.82	0.82	0.80	0.78	0.80	1.03
-0.5	0.76	0.87	0.89	0.90	0.90	0.89	0.88	0.88	0.86	0.86	0.84	0.83	0.83	0.82	0.81	0.80	0.79	0.80	1.06
-1.5	0.75	0.86	0.91	0.89	0.90	0.89	0.89	0.87	0.87	0.86	0.84	0.84	0.83	0.81	0.81	0.80	0.78	0.82	1.04
-2.5	0.76	0.83	0.96	0.87	0.89	0.89	0.88	0.87	0.86	0.86	0.84	0.84	0.83	0.82	0.81	0.79	0.77	0.87	1.05
-3.5	0.74	0.80	0.93	0.88	0.88	0.88	0.88	0.87	0.86	0.85	0.84	0.83	0.82	0.82	0.81	0.79	0.78	0.98	1.02
-4.5	0.73	0.82	0.87	0.94	0.88	0.88	0.88	0.87	0.86	0.85	0.85	0.84	0.83	0.82	0.80	0.79	0.88	1.01	1.01
-5.5	0.71	0.75	0.83	0.93	0.90	0.86	0.86	0.86	0.85	0.84	0.84	0.83	0.82	0.80	0.79	0.84	1.02	0.95	0.97
-6.5	0.74	0.79	0.81	0.87	0.96	0.94	0.86	0.84	0.84	0.84	0.83	0.83	0.80	0.80	0.88	1.01	1.01	0.92	0.92
-7.5	0.71	0.74	0.76	0.82	0.90	0.99	1.00	0.93	0.87	0.85	0.85	0.86	0.88	0.98	1.03	0.99	0.94	0.93	0.79
-8.5	0.71	0.72	0.77	0.79	0.86	0.90	0.94	0.99	0.99	1.01	1.00	1.03	0.99	0.98	0.98	0.96	0.92	0.82	0.79
-9.5	0.71	0.72	0.77	0.74	0.79	0.81	0.82	0.90	0.90	0.93	0.93	0.94	0.92	0.90	0.89	0.85	0.85	0.82	0.79

Figure 4c: On-DIC air kerma to water dose ((Gy s^{-1})/(Gy s^{-1})) conversion coefficients for the 0.2 mm Al filtered field at position (*x*,*y*) for shelf at *z*=-32.5 cm, 220 kV tube potential and 18.2 mA current.

(X,Y)	-9.5	-8.5	-7.5	-6.5	-5.5	-4.5	-3.5	-2.5	-1.5	-0.5	0.5	1.5	2.5	3.5	4.5	5.5	6.5	7.5	8.5
9.5	0.00	0.00	0.00	0.00	0.00	0.00	0.00	0.00	0.00	0.01	0.00	0.00	0.00	0.00	0.00	0.00	0.00	0.00	0.00
8.5	0.00	0.00	0.00	0.00	0.00	0.01	0.01	0.01	0.01	0.01	0.01	0.01	0.01	0.01	0.00	0.00	0.00	0.00	0.00
7.5	0.00	0.00	0.00	0.00	0.01	0.01	0.01	0.01	0.01	0.01	0.01	0.01	0.01	0.01	0.01	0.01	0.00	0.00	0.00
6.5	0.00	0.00	0.00	0.01	0.01	0.01	0.01	0.02	0.02	0.03	0.03	0.02	0.02	0.01	0.01	0.01	0.01	0.00	0.00
5.5	0.00	0.00	0.01	0.01	0.01	0.02	0.03	0.04	0.05	0.06	0.05	0.04	0.03	0.02	0.02	0.01	0.01	0.01	0.00
4.5	0.00	0.01	0.01	0.01	0.02	0.03	0.06	0.08	0.11	0.18	0.18	0.11	0.07	0.04	0.03	0.02	0.01	0.01	0.00
3.5	0.00	0.01	0.01	0.02	0.03	0.06	0.11	0.33	0.80	1.04	1.06	0.86	0.34	0.08	0.04	0.02	0.01	0.01	0.01
2.5	0.00	0.01	0.01	0.02	0.05	0.11	0.34	1.00	1.17	1.25	1.28	1.27	1.12	0.35	0.07	0.03	0.02	0.01	0.01
1.5	0.01	0.01	0.01	0.03	0.07	0.16	0.78	1.13	1.25	1.33	1.36	1.35	1.30	0.91	0.11	0.04	0.02	0.01	0.01
0.5	0.01	0.01	0.01	0.03	0.09	0.22	0.97	1.18	1.29	1.36	1.40	1.39	1.34	1.16	0.18	0.05	0.02	0.01	0.01
-0.5	0.01	0.01	0.02	0.03	0.09	0.21	0.97	1.18	1.29	1.35	1.39	1.39	1.34	1.15	0.18	0.05	0.02	0.01	0.01
-1.5	0.01	0.01	0.01	0.03	0.07	0.16	0.78	1.14	1.25	1.32	1.36	1.35	1.30	0.90	0.11	0.04	0.02	0.01	0.01
-2.5	0.00	0.01	0.01	0.02	0.05	0.11	0.34	0.99	1.17	1.24	1.28	1.27	1.13	0.34	0.07	0.03	0.02	0.01	0.01
-3.5	0.00	0.01	0.01	0.02	0.03	0.06	0.11	0.33	0.80	1.03	1.06	0.85	0.34	0.08	0.04	0.02	0.01	0.01	0.01
-4.5	0.00	0.01	0.01	0.01	0.02	0.03	0.06	0.08	0.12	0.18	0.18	0.11	0.07	0.04	0.03	0.02	0.01	0.01	0.00
-5.5	0.00	0.00	0.01	0.01	0.01	0.02	0.03	0.04	0.05	0.06	0.05	0.05	0.03	0.02	0.02	0.01	0.01	0.01	0.00
-6.5	0.00	0.00	0.00	0.01	0.01	0.01	0.01	0.02	0.02	0.03	0.03	0.02	0.02	0.01	0.01	0.01	0.01	0.00	0.00
-7.5	0.00	0.00	0.00	0.00	0.01	0.01	0.01	0.01	0.01	0.01	0.01	0.01	0.01	0.01	0.01	0.01	0.00	0.00	0.00
-8.5	0.00	0.00	0.00	0.00	0.00	0.00	0.01	0.01	0.01	0.01	0.01	0.01	0.01	0.01	0.00	0.00	0.00	0.00	0.00
-9.5	0.00	0.00	0.00	0.00	0.00	0.00	0.00	0.00	0.00	0.01	0.00	0.00	0.00	0.00	0.00	0.00	0.00	0.00	0.00

Figure 5a: On-DIC dose rates to water (Gy s^{-1}) for the 0.2 mm Al filtered field at position (*x*,*y*) for shelf at *z*=-22.6 cm, 220 kV tube potential and 18.2 mA current.

(X,Y)	-9.5	-8.5	-7.5	-6.5	-5.5	-4.5	-3.5	-2.5	-1.5	-0.5	0.5	1.5	2.5	3.5	4.5	5.5	6.5	7.5	8.5
9.5	0.00	0.00	0.00	0.00	0.00	0.00	0.00	0.00	0.00	0.00	0.00	0.00	0.00	0.00	0.00	0.00	0.00	0.00	0.00
8.5	0.00	0.00	0.00	0.00	0.00	0.00	0.00	0.01	0.01	0.01	0.01	0.01	0.01	0.00	0.00	0.00	0.00	0.00	0.00
7.5	0.00	0.00	0.00	0.00	0.00	0.01	0.01	0.01	0.01	0.01	0.01	0.01	0.01	0.01	0.01	0.00	0.00	0.00	0.00
6.5	0.00	0.00	0.00	0.00	0.01	0.01	0.01	0.02	0.03	0.03	0.03	0.02	0.02	0.01	0.01	0.01	0.00	0.00	0.00
5.5	0.00	0.00	0.00	0.01	0.01	0.01	0.02	0.03	0.05	0.05	0.05	0.04	0.03	0.02	0.01	0.01	0.01	0.00	0.00
4.5	0.00	0.00	0.01	0.01	0.01	0.03	0.06	0.08	0.11	0.19	0.19	0.10	0.06	0.04	0.02	0.01	0.01	0.01	0.00
3.5	0.00	0.00	0.01	0.01	0.02	0.06	0.12	0.38	0.98	1.29	1.35	1.11	0.42	0.07	0.04	0.02	0.01	0.01	0.00
2.5	0.00	0.01	0.01	0.02	0.05	0.12	0.39	1.19	1.40	1.52	1.59	1.61	1.47	0.43	0.06	0.03	0.02	0.01	0.01
1.5	0.00	0.01	0.01	0.03	0.08	0.18	0.93	1.35	1.49	1.60	1.67	1.70	1.67	1.21	0.10	0.04	0.02	0.01	0.01
0.5	0.00	0.01	0.01	0.05	0.11	0.25	1.15	1.38	1.54	1.64	1.72	1.75	1.72	1.55	0.19	0.04	0.03	0.01	0.01
-0.5	0.00	0.01	0.01	0.05	0.11	0.25	1.15	1.38	1.53	1.65	1.72	1.75	1.71	1.54	0.19	0.04	0.03	0.01	0.01
-1.5	0.00	0.01	0.01	0.04	0.08	0.18	0.92	1.34	1.48	1.60	1.67	1.70	1.66	1.21	0.10	0.04	0.02	0.01	0.01
-2.5	0.00	0.01	0.01	0.02	0.05	0.12	0.39	1.19	1.40	1.51	1.59	1.60	1.47	0.42	0.06	0.03	0.02	0.01	0.01
-3.5	0.00	0.00	0.01	0.01	0.02	0.06	0.12	0.38	0.98	1.29	1.35	1.10	0.41	0.07	0.04	0.02	0.01	0.01	0.00
-4.5	0.00	0.00	0.01	0.01	0.01	0.03	0.05	0.08	0.11	0.19	0.19	0.10	0.06	0.04	0.02	0.01	0.01	0.01	0.00
-5.5	0.00	0.00	0.00	0.01	0.01	0.01	0.02	0.03	0.05	0.05	0.05	0.04	0.03	0.02	0.01	0.01	0.01	0.00	0.00
-6.5	0.00	0.00	0.00	0.00	0.01	0.01	0.01	0.02	0.03	0.03	0.03	0.03	0.02	0.01	0.01	0.01	0.00	0.00	0.00
-7.5	0.00	0.00	0.00	0.00	0.00	0.01	0.01	0.01	0.01	0.01	0.01	0.01	0.01	0.01	0.01	0.00	0.00	0.00	0.00
-8.5	0.00	0.00	0.00	0.00	0.00	0.00	0.00	0.01	0.01	0.01	0.01	0.01	0.01	0.00	0.00	0.00	0.00	0.00	0.00
-9.5	0.00	0.00	0.00	0.00	0.00	0.00	0.00	0.00	0.00	0.00	0.00	0.00	0.00	0.00	0.00	0.00	0.00	0.00	0.00

Figure 5b: On-DIC air kerma rates (Gy s^{-1}) for the 0.2 mm Al filtered field at position (*x*,*y*) for shelf at *z*=-22.6 cm, 220 kV tube potential and 18.2 mA current.

(X,Y)	-9.5	-8.5	-7.5	-6.5	-5.5	-4.5	-3.5	-2.5	-1.5	-0.5	0.5	1.5	2.5	3.5	4.5	5.5	6.5	7.5	8.5
9.5	0.88	0.74	0.82	1.02	1.02	1.14	1.16	1.07	1.18	1.19	1.06	1.27	1.05	1.12	0.98	0.92	1.10	1.02	0.97
8.5	0.78	0.87	0.93	1.04	1.20	1.27	1.35	1.26	1.30	1.37	1.29	1.28	1.28	1.19	1.13	1.10	1.20	1.04	0.82
7.5	1.06	1.06	1.08	1.24	1.28	1.38	1.43	1.33	1.16	1.19	1.12	1.23	1.28	1.26	1.28	1.29	1.31	1.11	1.02
6.5	0.96	1.15	1.24	1.29	1.47	1.45	1.42	1.09	0.89	0.80	0.86	0.89	1.05	1.34	1.46	1.39	1.34	1.20	1.10
5.5	1.07	1.17	1.30	1.47	1.50	1.43	1.29	1.12	1.03	1.04	1.09	1.15	1.22	1.34	1.46	1.53	1.50	1.38	1.24
4.5	1.19	1.33	1.37	1.44	1.45	1.20	1.01	1.00	1.03	0.94	0.94	1.09	1.20	1.21	1.33	1.47	1.51	1.41	1.29
3.5	1.16	1.34	1.30	1.27	1.17	0.95	0.94	0.86	0.82	0.80	0.79	0.77	0.82	1.17	1.23	1.36	1.38	1.45	1.39
2.5	1.13	1.30	1.29	1.06	0.97	0.87	0.86	0.84	0.83	0.82	0.80	0.79	0.76	0.81	1.23	1.27	1.17	1.30	1.27
1.5	1.18	1.43	1.20	0.84	0.86	0.86	0.84	0.84	0.84	0.83	0.81	0.79	0.78	0.75	1.12	1.20	0.90	1.24	1.39
0.5	1.27	1.43	1.09	0.65	0.80	0.86	0.84	0.85	0.84	0.82	0.81	0.80	0.78	0.75	0.92	1.16	0.83	1.17	1.33
-0.5	1.26	1.45	1.08	0.64	0.80	0.85	0.84	0.85	0.84	0.82	0.81	0.80	0.78	0.75	0.92	1.21	0.81	1.18	1.36
-1.5	1.22	1.31	1.05	0.76	0.87	0.87	0.84	0.85	0.84	0.82	0.81	0.79	0.78	0.75	1.13	1.18	0.90	1.24	1.33
-2.5	1.24	1.38	1.26	1.06	0.97	0.86	0.86	0.83	0.84	0.82	0.80	0.79	0.77	0.81	1.20	1.24	1.16	1.38	1.32
-3.5	1.17	1.26	1.39	1.36	1.17	0.96	0.96	0.87	0.81	0.80	0.79	0.78	0.82	1.19	1.24	1.36	1.33	1.38	1.27
-4.5	1.16	1.27	1.43	1.47	1.44	1.20	1.04	1.01	1.05	0.94	0.93	1.08	1.20	1.21	1.34	1.46	1.43	1.38	1.29
-5.5	1.13	1.26	1.32	1.48	1.55	1.45	1.23	1.08	1.04	1.05	1.07	1.14	1.28	1.31	1.42	1.53	1.45	1.30	1.16
-6.5	0.93	1.07	1.18	1.36	1.39	1.51	1.22	1.02	0.82	0.85	0.78	0.88	1.14	1.29	1.51	1.44	1.33	1.23	1.15
-7.5	0.97	1.10	1.16	1.25	1.32	1.40	1.35	1.23	1.13	1.21	1.10	1.29	1.27	1.39	1.29	1.37	1.21	1.07	0.99
-8.5	0.91	1.00	1.00	1.09	1.22	1.24	1.32	1.34	1.42	1.36	1.31	1.40	1.31	1.34	1.22	1.27	1.16	1.02	0.91
-9.5	0.86	0.85	0.87	1.02	1.01	1.07	1.13	1.25	1.25	1.19	1.13	1.22	1.15	1.16	1.04	1.03	1.14	0.99	0.82

Figure 5c: On-DIC air kerma to water dose ((Gy s^{-1})/(Gy s^{-1})) conversion coefficients for the 0.2 mm Al filtered field at position (*x*,*y*) for shelf at *z*=-22.6 cm, 220 kV tube potential and 18.2 mA current.

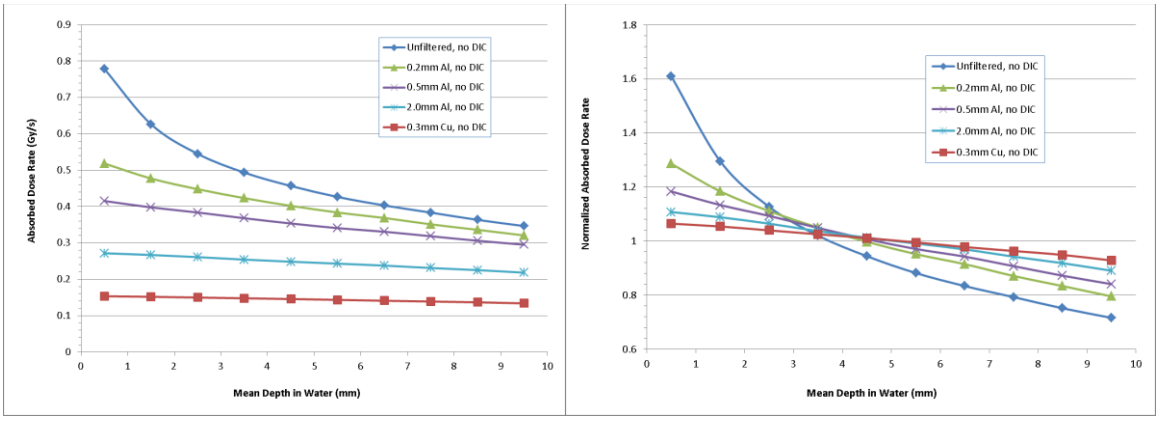

Figure 6: Depth-dose profile through 1 cm of water at a central location on-shelf at *z*=-22.6 cm, for 220 kV tube potential and 18.2 mA current: (*Left*) Absolute dose rates; (*Right*)dose rates self-normalized to the mean over the whole 1 cm^3 volume.

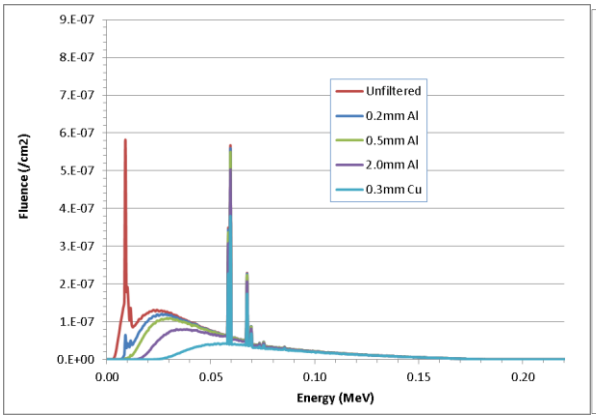

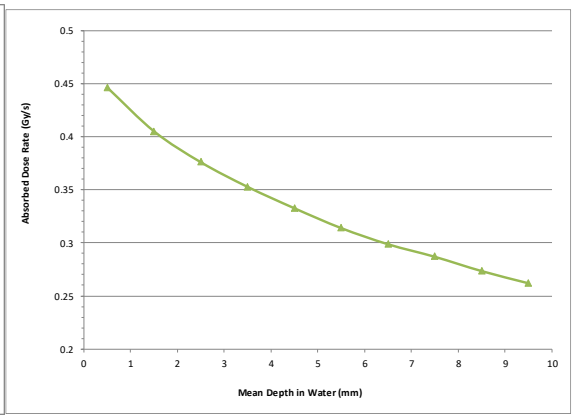

(X,Y)	-9.5	-8.5	-7.5	-6.5	-5.5	-4.5	-3.5	-2.5	-1.5	-0.5	0.5	1.5	2.5	3.5	4.5	5.5	6.5	7.5	8.5	9.5
9.5	0.00	0.01	0.01	0.01	0.01	0.01	0.01	0.01	0.01	0.01	0.01	0.01	0.01	0.01	0.01	0.01	0.00	0.00	0.00	0.00
8.5	0.01	0.01	0.01	0.01	0.01	0.01	0.01	0.02	0.02	0.03	0.03	0.03	0.02	0.01	0.01	0.01	0.01	0.01	0.00	0.00
7.5	0.01	0.01	0.01	0.01	0.01	0.02	0.03	0.06	0.10	0.12	0.12	0.10	0.07	0.04	0.02	0.01	0.01	0.01	0.00	0.00
6.5	0.01	0.01	0.01	0.02	0.02	0.06	0.13	0.20	0.23	0.24	0.24	0.24	0.21	0.15	0.07	0.03	0.01	0.01	0.01	0.00
5.5	0.01	0.02	0.02	0.03	0.07	0.17	0.23	0.26	0.27	0.28	0.29	0.29	0.28	0.25	0.19	0.09	0.03	0.01	0.01	0.01
4.5	0.02	0.02	0.02	0.05	0.17	0.24	0.26	0.28	0.29	0.30	0.31	0.31	0.31	0.30	0.27	0.20	0.07	0.02	0.01	0.01
3.5	0.02	0.02	0.03	0.13	0.23	0.26	0.28	0.29	0.31	0.31	0.32	0.32	0.32	0.33	0.30	0.27	0.15	0.04	0.01	0.01
2.5	0.02	0.03	0.05	0.19	0.25	0.27	0.29	0.30	0.32	0.32	0.33	0.33	0.33	0.32	0.32	0.30	0.22	0.07	0.02	0.01
1.5	0.02	0.03	0.08	0.22	0.26	0.28	0.29	0.31	0.32	0.33	0.33	0.34	0.34	0.33	0.33	0.31	0.26	0.11	0.02	0.01
0.5	0.02	0.03	0.10	0.23	0.26	0.28	0.30	0.31	0.32	0.33	0.33	0.34	0.34	0.33	0.33	0.31	0.28	0.13	0.03	0.01
-0.5	0.02	0.03	0.10	0.23	0.26	0.28	0.30	0.31	0.32	0.33	0.34	0.34	0.34	0.33	0.33	0.32	0.28	0.13	0.03	0.01
-1.5	0.02	0.03	0.08	0.22	0.26	0.28	0.29	0.31	0.32	0.33	0.33	0.34	0.34	0.33	0.32	0.31	0.26	0.11	0.02	0.01
-2.5	0.02	0.03	0.05	0.19	0.25	0.27	0.29	0.30	0.31	0.32	0.33	0.33	0.33	0.33	0.32	0.30	0.22	0.07	0.02	0.01
-3.5	0.02	0.02	0.03	0.13	0.23	0.26	0.28	0.30	0.31	0.32	0.32	0.32	0.32	0.31	0.30	0.27	0.15	0.04	0.01	0.01
-4.5	0.02	0.02	0.02	0.05	0.17	0.24	0.26	0.28	0.29	0.30	0.31	0.31	0.30	0.30	0.27	0.20	0.07	0.02	0.01	0.01
-5.5	0.01	0.02	0.02	0.03	0.07	0.17	0.23	0.26	0.27	0.28	0.29	0.29	0.28	0.26	0.19	0.09	0.03	0.01	0.01	0.01
-6.5	0.01	0.01	0.01	0.02	0.02	0.06	0.13	0.19	0.23	0.24	0.24	0.24	0.21	0.15	0.07	0.03	0.02	0.01	0.01	0.00
-7.5	0.01	0.01	0.01	0.01	0.01	0.02	0.03	0.06	0.10	0.12	0.12	0.10	0.07	0.04	0.02	0.01	0.01	0.01	0.00	0.00
-8.5	0.01	0.01	0.01	0.01	0.01	0.01	0.01	0.02	0.02	0.03	0.03	0.02	0.02	0.02	0.01	0.01	0.01	0.00	0.00	0.00
-9.5	0.00	0.01	0.01	0.01	0.01	0.01	0.01	0.01	0.01	0.01	0.01	0.01	0.01	0.01	0.01	0.01	0.00	0.00	0.00	0.00

Figure 7: Results for a 190 kV tube potential and 18.2 mA current. (*Top left*) Filtered and unfiltered photon fields; (*Top right*) Depth-dose profile through 1 cm of water at a central location on-shelf at z = -22.6 cm for 0.2 mm Al filter; (*Bottom*) On-shelf dose rates to water (Gy s^{-1}) for the 0.2 mm Al filtered field at position (x,y).

Table 1: Mean energies of the 190 kV and 220 kV filtered and unfiltered fields.

Potential (kV)	**Mean Energy (keV)**				
	Unfiltered	*0.2 mm Al*	*0.5 mm Al*	*2.0 mm Al*	*0.3 mm Cu*
190	39.5	47.0	50.5	58.5	67.5
220	45.0	51.5	55.0	59.5	70.0